Journal of Business, Social and Technology
Volume 7, Issue 6, 2882-2893
e_ISSN: 2807-6362
https://bustechno.polteksci.ac.id/index.php/jbt/index
DOI: https://doi.org/10.59261/bustechno.v7i6.858

Integrated Diagnosis of Calcite Scaling in Well X at an Indonesian Geothermal Field

Akhmad Sofyan[1*]
Politeknik Energi dan Mineral Akamigas, Indonesia

Trisya Amanda Nur Rahma[2]
Politeknik Energi dan Mineral Akamigas, Indonesia

Kristofol Waas[3]
Politeknik Negeri Ambon, Indonesia

***Corresponding author:**
Akhmad Sofyan, Politeknik Energi dan Mineral Akamigas, Indonesia.
✉akhmads@esdm.go.id

Article Info:
Article history:
Received: October 03, 2026
Revised: November 16, 2026
Accepted: November 18, 2026
Available Online: November 19, 2026

Keywords:
Calcite Scaling;
Geothermal Well;
PHREEQC;
Thermodynamically Sensitive Interval;
Wellbore Restriction

This is an open access article under the CC BY-SA license.

Copyright © 2026 by Author. Published by Politeknik Siber Cerdika International

Abstract

Background: Mineral precipitation reduces geothermal well productivity by narrowing the effective flow area and increasing hydraulic resistance.
Objective: This study investigates production impairment in Well X at an anonymized geothermal field in West Java, Indonesia.
Methods: A retrospective, single-well diagnosis was conducted by integrating exponential decline-curve fitting, pressure–temperature–spinner logging, WellSim simulation, PHREEQC output, hydraulic scenario analysis, X-ray diffraction (XRD), and downhole video inspection.
Results: Decline-curve fitting yielded a decline coefficient (D) of 0.0035 day^{-1}, an initial production rate (q_i) of 25.33 t/h, and an R^2 of 0.3825, indicating a limited model fit without ruling out reservoir depletion. Temperature profiles converged near 1,000 m measured depth (MD). Because mist flow and high steam mass fractions were observed throughout the modeled interval, the 950–1,050 m interval was interpreted as thermodynamically sensitive and prone to scaling, rather than as the initial flashing point. The supplied PHREEQC output indicated calcite supersaturation; however, incomplete model reconstruction and unmatched pressure–temperature conditions limit its applicability to downhole interpretation. A hydraulic scenario involving simultaneous changes in pipe diameter and wall roughness increased the combined frictional and accelerational pressure gradient from 211.67 to 317.32 Pa/m. XRD confirmed the presence of calcite, while downhole video revealed mineral deposition near 975 m; sample recovery was reported separately at approximately 984 m.
Conclusion: The integrated diagnosis supports calcite scaling as a major contributor to production impairment. However, its contribution cannot be isolated from the effects of reservoir depletion or operational changes.

To cite this article: Sofyan, A., Rahma, T. A. N., & Waas, K. (2026). Integrated Diagnosis of Flashing-Induced Precipitation in Well X of the Geothermal Field, Indonesia. *Journal of Business, Social and Technology, 7*(6), 2882–2893. https://doi.org/10.59261/bustechno.v7i6.858

INTRODUCTION

Geothermal energy plays an important role in sustainable energy development, particularly in countries such as Indonesia, which possesses substantial geothermal resources. However, the long-term utilization of geothermal energy depends not only on reservoir capacity but also on the ability to maintain stable and efficient well performance (Sofyan et al., 2023). One of the most common operational challenges in geothermal production systems is mineral scaling, which can reduce the internal flow area, increase pressure losses, and ultimately decrease production capacity (Sofyan et al., 2025).

Scaling occurs when geothermal fluids undergo changes in pressure, temperature, phase conditions, and dissolved gas composition as they flow from the reservoir to the surface (Hassani & Zheng, 2025). These changes can disturb chemical equilibrium and trigger mineral precipitation within the wellbore and surface facilities. In carbonate-bearing geothermal systems, calcite is particularly important because depressurization and CO_2 degassing tend to increase pH and shift carbonate equilibrium toward supersaturation. This mechanism is especially significant in wells that undergo flashing, as phase separation and gas release can alter fluid chemistry and promote mineral deposition within the wellbore.

Operational evidence from other geothermal fields illustrates the importance of distinguishing between potential scaling mechanisms. At Ngatamariki, unexpectedly rapid production declines in two of three operating production wells prompted an investigation that identified calcite deposition despite an initially low assessed scaling risk (Quinao et al., 2017). In southern Germany, Wanner et al. (2017) combined fluid, scale, and gas-inclusion analyses to evaluate several possible drivers of mineral precipitation, demonstrating why a single saturation calculation is insufficient to distinguish among different scaling mechanisms. Mineral deposits can also interact with corrosion products and develop rough surfaces that increase flow resistance and promote the mobilization of scale fragments (Boch et al., 2017).

In practice, identifying scaling as the primary cause of production decline is not always straightforward. A reduction in well output can also result from natural reservoir depletion, changes in feed-zone contributions, or mechanical restrictions unrelated to mineral precipitation (Jamero et al., 2018). Therefore, scaling cannot be reliably diagnosed using a single indicator. A more robust interpretation requires the integration of production behavior, wellbore thermal conditions, fluid geochemistry, hydraulic response, and direct field observations.

In Indonesia, Sofyan et al. (2025) investigated broaching treatment planning for a vapor-dominated well at Kamojang, illustrating the operational importance of identifying internal restrictions before selecting intervention methods. Sujarmaitanto et al. (2024) integrated downhole observations and geochemical analyses at Patuha, demonstrating that a predominantly vapor-producing system may still contain liquid requiring chemical characterization. These studies provide contextual examples from previously investigated geothermal fields rather than identifying the anonymized Well X examined in the present study. They support a diagnostic approach that distinguishes bulk steam conditions from the chemical characteristics of the residual liquid and the physical presence of mineral deposits.

Allan et al. (2019) combined wellbore simulation and downhole surveys at Ngatamariki to interpret scale geometry and changes in well performance, thereby supporting intervention planning. Cao et al. (2024) coupled thermal, hydraulic, and chemical calculations to predict locations of fluid flashing and calcite deposition, comparing their predictions with field observations. Bu et al. (2022) combined scaling analysis, simulation, and field testing of antiscalants. These studies demonstrate that scale localization and its operational effects have previously been investigated together. The contribution of the present study lies in integrating these diagnostic elements for the specific case of Well X, rather than proposing the first causal framework for geothermal scaling.

The diagnostic challenge in Well X involves interpreting a declining and variable production record alongside evidence of a localized mineral deposit. Figure 1 presents 35 plotted observations spanning elapsed days 14 to 365; however, no calendar dates or synchronized operating logs are available. A weak exponential fit alone cannot establish the underlying cause of production decline. The specific research question is whether the mineralogical, visual, thermodynamic, and hydraulic evidence consistently supports calcite scaling as a contributing factor while accounting for alternative reservoir-related and operational explanations.

This study integrates production decline fitting, WellSim temperature-profile comparisons, PHREEQC saturation calculations, and hydraulic scenario analyses. X-ray diffraction (XRD) and downhole video surveys provide complementary mineralogical and visual evidence. The objective is to assess the contribution of calcite scaling to production impairment and identify a probable deposition-sensitive interval within the well. The anticipated operational benefit is to inform targeted inspections and the design of subsequent scale-management assessments. However, the study does not establish a transferable predictive model or quantify the proportion

of production loss attributable to scaling.

An additional consideration is the distinction between thermodynamic precipitation potential and the actual mass of deposited minerals. Köhl et al. (2020) compared scale measurements with hydrochemical models, demonstrating the importance of evaluating precipitation kinetics against physical measurements. Hörbrand et al. (2018) evaluated hydrogeochemical databases under geothermal conditions, while Lu et al. (2022) documented differences among PHREEQC thermodynamic databases. Shoeibi Omrani et al. (2025) incorporated compositional uncertainty into coupled scaling and hydraulic assessments. These findings underscore the need for conservative interpretation and the recovery of missing Well X input data before the results are used for predictive purposes.

METHOD

Study Area

This retrospective, observational case study examined Well X at an anonymized geothermal field in West Java, Indonesia. The integrated dataset comprised production history, pressure–temperature–spinner (PTS) logging, downhole sampling (DHS), downhole video (DHV), X-ray diffraction (XRD), and fluid geochemistry. Published field names cited for contextual purposes do not disclose the identity of Well X.

PTS profiles were interpreted to assess thermal behavior and compared with simulated saturation temperatures. DHS chemistry represented the sampled liquid, whose composition may differ from that of surface fluids following phase separation. Mineralogical and visual observations were assessed separately, consistent with the complementary use of downhole and geochemical evidence demonstrated by (Sujarmaitanto et al., 2024).

Production Decline Analysis

Production decline analysis was used as the initial diagnostic step to evaluate whether the reduction in well output could be explained by natural depletion alone. The analysis followed the exponential decline relationship introduced by Arps (Wahba et al., 2022):

$$q = q_i e^{-Dt} \quad (1)$$

which can be rewritten in linear form as:

$$ln(q) = ln(q_i) - Dt \quad (2)$$

where q is the production rate at time t, q is the initial production rate, and D is the decline constant. Linear regression was applied to estimate the rate of decline and examine whether the observed production behavior followed a simple natural decline pattern. In this study, decline analysis was used primarily as an early diagnostic tool rather than as a long-term forecasting method.

Thermal-Hydraulic Wellbore Simulation

Thermal-hydraulic simulation was performed using WellSim and the reported casing and liner geometry, extending from a measured depth of 1,700 m to the wellhead. The reported profiles of pressure, temperature, steam mass fraction, flow rate, and flow regime were compared with the PTS temperature measurements. Such comparisons can support the interpretation of two-phase well conditions Lei et al. (2023), but do not, by themselves, demonstrate model calibration.

Allan et al. (2019) used wellbore simulation together with downhole evidence to assess calcite deposition. In this study, the supplied WellSim results were interpreted diagnostically. However, the software version, specified boundary conditions, feed-zone allocation, flow correlation, and calibration residuals were unavailable; therefore, the calculations are not presented as independently reproducible or validated.

The measured and simulated temperature profiles were compared to identify a thermodynamically sensitive interval near the point of convergence. The presence of mist flow and a steam mass fraction of 0.980 at the deepest modeled depth already indicates two-phase

conditions. Thus, profile convergence near 1,000 m cannot establish the initial onset of flashing. The 950–1,050 m interval represents a qualitative interpretation based on the convergence region, rather than a statistical confidence interval or a model-derived phase boundary.

Geochemical Saturation Modeling

The supplied output from PHREEQC Version 3 was reviewed to assess mineral saturation. PHREEQC performs aqueous speciation and equilibrium calculations (U.S. Geological Survey, 2025), and its results depend on the selected thermodynamic database and solution definition (Lu et al., 2022). The saturation index (SI) was defined as:

$$SI = log_{10}(IAP/K) \quad (3)$$

where IAP is the ion activity product and K is the equilibrium constant for the specified mineral reaction at the calculation temperature and pressure.

A positive SI indicates supersaturation, an SI of zero indicates equilibrium, and a negative SI indicates undersaturation. Supersaturation indicates thermodynamic potential for precipitation, rather than the precipitation rate or the amount of accumulated scale. Table 3 reports a field pH of 8.1, a laboratory pH of 6.2, a temperature of 235 °C, and selected components in ppm. The unit ppm was retained as reported because the underlying mass- or volume-based concentration convention was unspecified.

The thermodynamic database, complete analytical composition, alkalinity/carbon input convention, charge-balance error, pH correction, and gas-equilibration settings were not provided. Figure 3 explicitly reports a temperature of 527 K (253.85 °C) and a pressure of 5 atm (approximately 0.507 MPa absolute), which differ from the values reported in Table 3 and the approximately 1.5 MPa WellSim pressure near 1,000 m. No documented fluid reconstruction links these conditions. Therefore, the SI values are reported as supplied model outputs rather than as validated in situ values. The field and laboratory pH measurements cannot be interchanged or interpreted as constituting a completed degassing sensitivity experiment. The suitability of the thermodynamic database and the sensitivity of the results require verification before the model can be used for downhole (Hörbrand et al., 2018).

Hydraulic Restriction Assessment

The reported unrestricted and restricted scenarios were compared using the results presented in Table 4. The diameter of the 10¾-inch section changed from 0.247904 to 0.1016 m, while the roughness was set to 0.001 m in all listed sections. Consequently, the comparison combines the effects of changes in diameter and roughness. The frictional and accelerational pressure gradients were summed to provide a local hydraulic indicator. However, without information on the restriction length or calibrated discharge curves, neither the integrated pressure loss nor the reduction in production rate was calculated. The hydraulic response is also influenced by the two-phase fluid composition (Khasani et al., 2021).

Review of Published XRD and Downhole Video Evidence

The case analysis used the reported production series, pressure–temperature–spinner (PTS) temperature data, downhole fluid chemistry, and model outputs for Well X. Published X-ray diffraction (XRD) and downhole video (DHV) evidence from the Patuha geothermal field was reviewed for comparative purposes. The source identifies the illustrated well as HND-C Sujarmaitanto et al. (2024) Figure 15. However, a documented link between those records and the anonymized Well X dataset was unavailable. The manuscript also reports scale recovery at approximately 984 m measured depth, for which the original recovery log and specimen identifier were unavailable.

RESULTS AND DISCUSSION

Results

Production Decline Analysis

The decline curve analysis yielded the following regression equation:

$$y = -0.0035x + 3.2319 \quad (4)$$

The fit yielded $R^2 = 0.3825$, $D = 0.0035$ day^{-1}, and $q_i \approx 25.33$ t/h. Table 1 reports the fitted parameters and Figure 1 shows the production trend. These values describe the supplied fit and do not independently identify a physical decline mechanism.

Table 1
Decline curve analysis results

Decline Curve Analysis	Decline rate	Initial rate (qi)	
y = -0,0035x + 3,2319	Slope = -0,0035	Intercept =	3,2319
R^2 = 0,3825	D= 0,0035	25,327734	ton/hr

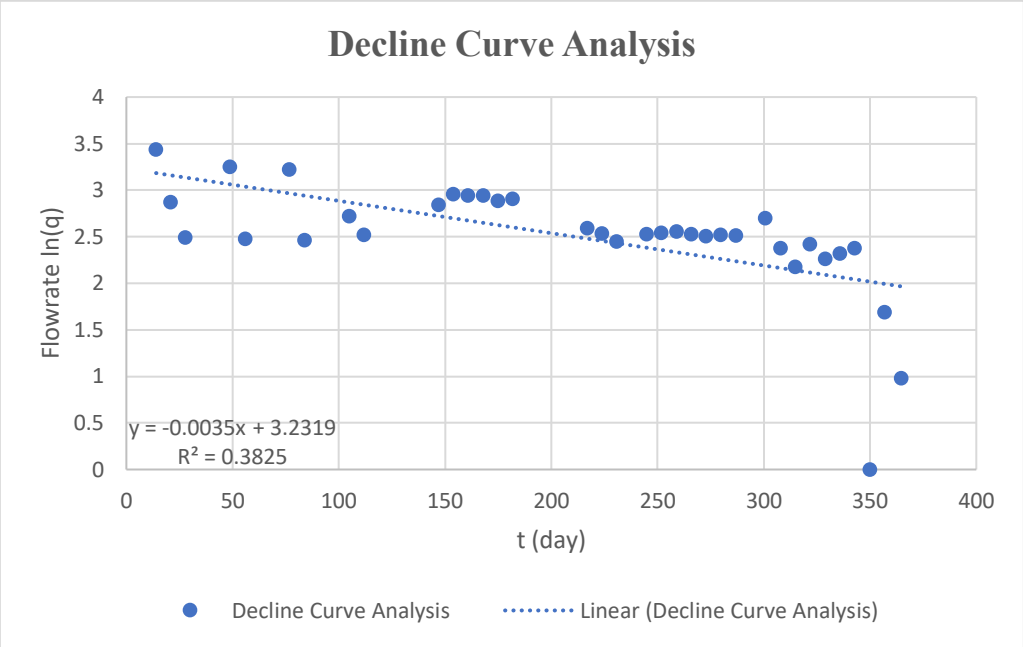


Figure 1. Decline Curve Analysis

As shown in Figure 1, the production measurements exhibit substantial deviations from the exponential regression. The R^2 value of 0.3825 indicates that approximately 38.3% of the variation in the logarithmic production rate is represented by the linear time trend. Therefore, the exponential model provides a relatively weak representation of the observed production behavior.

Thermal-Hydraulic Wellbore Simulation

The measured pressure–temperature–spinner (PTS) and simulated saturation-temperature profiles approached one another near 1,000 m measured depth (MD) (Figure 2). The surrounding interval of 950–1,050 m was interpreted as thermodynamically sensitive and potentially prone to scaling. Table 2 indicates persistent mist flow and high steam mass fractions throughout the modeled interval, preventing the identification of an initial flashing point from this comparison. At 1,700 m MD, the reported simulation outputs were an absolute pressure of 1.667 MPa, a temperature of 203.52 °C, a steam mass fraction of 0.980, and a mass flow rate of 4.775 kg/s. At the wellhead, the corresponding values were 1.384 MPa absolute, 194.67 °C, 0.956, and 9.551 kg/s, respectively. The depth-dependent changes in flow rate are consistent with modeled inflow contributions, although their individual allocations are not documented.

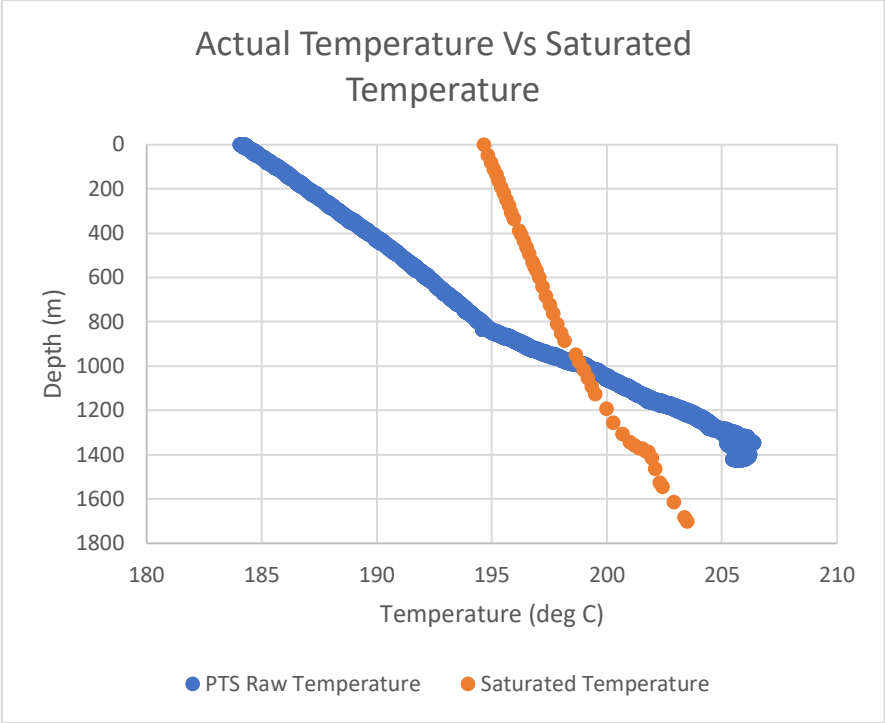


Figure 2. Temperature Comparison

Table *2*
WellSim discharge simulation results

Measured Depth [m]	Vertical Depth [m]	Pressure [Paa]	Temper-ature [deg C]	Fluid Dryness [mass ratio]	Mass Flowrate [kg/s]	Flow Regime
1700	1415,024637	1666666	203,5177928	0,98	4,775	Mist
1682	1402,07652	1662475,259	203,3955397	0,979980321	4,775	Mist
1613,070076	1352,07652	1646356,961	202,9230892	0,979899738	4,775	Mist
1544,140153	1302,07652	1630198,532	202,445839	0,979831136	4,775	Mist
1526	1288,918118	1625939,54	202,3194346	0,979811986	4,775	Mist
1462,549089	1238,918118	1619360,971	202,1236794	0,979644636	4,775	Mist
1415	1201,448925	1614436,038	201,9767254	0,979515963	4,775	Mist
1389	1180,960645	1609180,183	201,819512	0,925345174	5,2294	Mist
1385	1177,808602	1606012,413	201,7245645	0,941397095	6,5952	Mist
1373	1168,352473	1600874,742	201,570263	0,948858514	7,5059	Mist
1371	1166,776452	1596041,962	201,4247664	0,955514896	8,5534	Mist
1359,159644	1157,320323	1589634,368	201,2313287	0,956295156	8,69	Mist
1343,372502	1144,712151	1582339,413	201,0103628	0,95750806	8,9176	Mist
1307,811522	1116,311889	1571929,078	200,6936544	0,957950299	9,0085	Mist
1255,811522	1074,782843	1558661,709	200,2876534	0,959006517	9,2353	Mist
1191,811522	1025,398869	1549157,962	199,9951681	0,958871207	9,2353	Mist
1127,013172	975,3988695	1533608,925	199,5136077	0,959633666	9,4112	Mist
1093,811522	949,77966	1528644,514	199,3590572	0,959561963	9,4112	Mist
1055,811522	920,5636704	1522979,146	199,1822065	0,959488938	9,4112	Mist
1018,811522	891,6071686	1517403,219	199,0076469	0,959405529	9,4112	Mist
980,811522	862,391179	1511745,093	198,8300025	0,959321019	9,4112	Mist
947,811522	836,654991	1506789,104	198,6739766	0,959247048	9,4112	Mist
885,4093229	786,654991	1491227,939	198,1814631	0,959822381	9,5507	Mist
854,21157	761,6576726	1486434,565	198,0289456	0,959749718	9,5507	Mist
810,21157	725,5052073	1481133,992	197,8598429	0,959623073	9,5507	Mist

Measured Depth [m]	Vertical Depth [m]	Pressure [Paa]	Temper-ature [deg C]	Fluid Dryness [mass ratio]	Mass Flowrate [kg/s]	Flow Regime
763,21157	687,0050612	1475493,423	197,6793747	0,959486747	9,5507	Mist
724,21157	655,8582764	1470915,229	197,5325011	0,959375663	9,5507	Mist
683,21157	623,7713419	1466186,67	197,3804292	0,959261283	9,5507	Mist
643,21157	592,2509118	1461552,279	197,2310144	0,959148255	9,5507	Mist
600,21157	557,9095848	1456520,847	197,0683801	0,959024929	9,5507	Mist
571,21157	534,4778782	1453098,278	196,9574997	0,958941339	9,5507	Mist
551,21157	517,9953544	1450700,76	196,8797064	0,958881617	9,5507	Mist
531,21157	501,3756651	1448288,148	196,8013221	0,958820453	9,5507	Mist
494,21157	470,1355318	1443769,288	196,6542327	0,958705944	9,5507	Mist
463,21157	443,2617326	1439903,291	196,5281089	0,958607257	9,5507	Mist
434,21157	417,6325293	1436231,159	196,408065	0,958439502	9,5507	Mist
408,21157	394,0877405	1432873,151	196,2980803	0,958352735	9,5507	Mist
389,21157	376,5595168	1430382,529	196,2163752	0,958287033	9,5507	Mist
335,4722579	326,5595168	1423295,821	195,9832863	0,958099135	9,5507	Mist
335,21157	326,3169682	1423261,473	195,9821544	0,958098216	9,5507	Mist
307,21157	300,1592429	1420078,692	195,877173	0,957989405	9,5507	Mist
278,21157	272,7064144	1416742,572	195,7669366	0,95787326	9,5507	Mist
250,21157	245,9876852	1413499,324	195,6595747	0,95776143	9,5507	Mist
221,21157	217,9369203	1410098,72	195,5467973	0,957643371	9,5507	Mist
193,21157	190,676711	1406797,499	195,4371127	0,957515748	9,5507	Mist
165,21157	163,2291182	1403477,111	195,3265886	0,957398642	9,5507	Mist
137,21157	135,6545011	1400145,635	195,2154901	0,957348032	9,5507	Mist
111,21157	109,8595188	1397030,612	195,1114232	0,956971306	9,5507	Mist
81,21156997	79,95199882	1393419,193	194,9905458	0,956841177	9,5507	Mist
48,21156997	46,98597002	1389442,951	194,8571743	0,956698357	9,5507	Mist
0	0	1383783,529	194,6668309	0,956490041	9,5507	Mist

Geochemical Saturation Modeling

The supplied PHREEQC output reported saturation indices (SIs) of 2.10 for calcite, 0.77 for aragonite, and 1.94 for dolomite (Figure 3). These numerical values provide an indication of the reported supersaturation with respect to the carbonate minerals. However, they refer to the displayed calculation at 527 K and 5 atm. The mismatch between these conditions and the data presented in Tables 2 and 3 prevents the results from being directly associated with the proposed deposition interval. Calcite is supported by the mineralogical evidence, whereas positive SIs for the other phases do not independently establish their deposition.

Table 3

Geochemical input data

Downhole Sampling		
pH Field	8,1	-
pH Lab	6,2	-
Temp.	235	Celcius
Na	41	Ppm
Ca	49	Ppm
Mg	0,31	Ppm
Si	201	Ppm
B	9	Ppm
Cl	5	Ppm
HCO_3	51	Ppm

```
-----------------------------Saturation indices--------------------------------

  Phase               SI** log IAP   log K(527 K,   5 atm)

  Aragonite          0.77    -11.93  -12.70  CaCO3
  Calcite            2.10    -11.93  -14.03  CaCO3
  Chalcedony         1.45     -0.60   -2.05  SiO2
  Chrysotile         9.44     25.23   15.79  Mg3Si2O5(OH)4
  CO2(g)            -2.73     -4.67   -1.94  CO2
  Dolomite           1.94    -26.30  -28.25  CaMg(CO3)2
  H2(g)            -25.12    -27.71   -2.59  H2
  H2O(g)             0.59     -0.96   -1.55  H2O
  Halite            -8.29     -6.61    1.68  NaCl
  O2(g)              5.54      2.92   -2.62  O2
  Quartz             1.47     -0.60   -2.07  SiO2
  Sepiolite          1.38     13.74   12.36  Mg2Si3O7.5OH:3H2O
  Sepiolite(d)      -4.92     13.74   18.66  Mg2Si3O7.5OH:3H2O
  SiO2(a)            1.05     -0.60   -1.65  SiO2
  Talc              18.35     24.99    6.65  Mg3Si4O10(OH)2

**For a gas, SI = log10(fugacity). Fugacity = pressure * phi / 1 atm.
  For ideal gases, phi = 1.

-----------------
End of simulation.
-----------------

-----------------------------------
Reading input data for simulation 2.
-----------------------------------

-------------------------------
End of Run after 0.189 Seconds.
-------------------------------
```

Figure 3. Saturation Indices

Hydraulic Restriction Assessment

In the reported combined restriction-and-roughness scenario, the frictional pressure gradient increased from 209.855 to 314.783 Pa/m, while the accelerational pressure gradient increased from 1.814 to 2.540 Pa/m (Table 4). The corresponding total pressure gradients were 211.67 and 317.32 Pa/m, respectively. These values represent simulation outputs rather than directly measured pressure losses or statistically tested differences. Because the inner diameter and wall roughness were modified simultaneously, their individual effects cannot be isolated.

Table 4
Outflow comparison

Parameter	Before Restriction		After Restriction	
Inner Diameter (m)	20”	0,475742	20”	0,475742
	13-3/8”	0,315341	13-3/8”	0,315341
	10-3/4”	0,247904	10-3/4”	0,1016
	7”	0,1570736	7”	0,1570736
Roughness (m)	20”	0,000045	20”	0,001
	13-3/8”	0,000045	13-3/8”	0,001
	10-3/4”	0	10-3/4”	0,001
	7”	0	7”	0,001
Frictional dp/dz (Pa/m)	209,8553998		314,7830998	
Accelerational dp/dz (Pa/m)	1,814204313		2,539886038	
Flow Regime	Mist		Mist	

XRD and Downhole Video Observations

The published XRD pattern in Figure 4 identifies calcite among the mineral phases present in the HND-C sample. The published downhole video (DHV) image in Figure 5 shows a deposit on the perforated liner of HND-C at 975.71 m measured depth (Sujarmaitanto et al., 2024). The separately reported recovery depth of approximately 984 m could not be linked to the illustrated specimen or video footage using the available records.

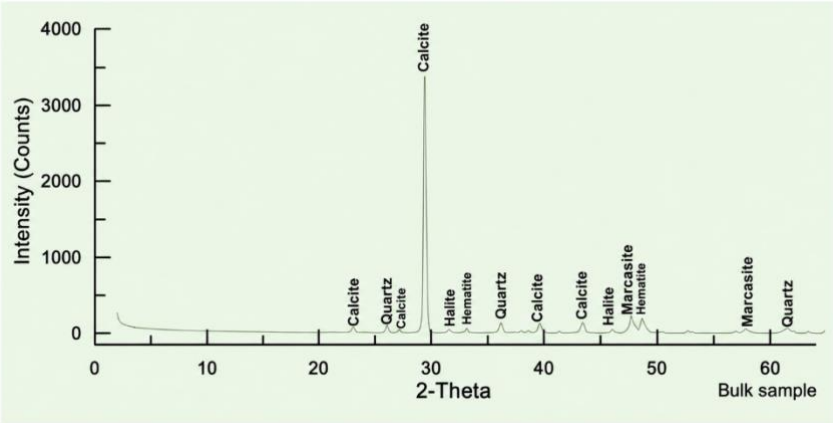


Figure 4. XRD analysis result (adapted from Sujarmaitanto et al., 2024, Figure 15a)

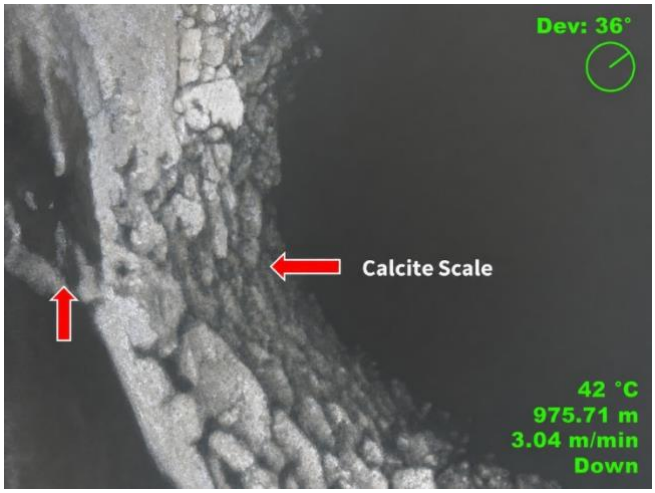


Figure 5. Downhole video result (adapted from Sujarmaitanto et al., 2024, Figure 15b)

The published DHV image shows mineral deposition at approximately 975 m measured depth (Sujarmaitanto et al., 2024). The original manuscript separately reports scale recovery at approximately 984 m measured depth, although the underlying recovery log was not provided. Both depths fall within the interpreted thermodynamically sensitive interval of 950–1,050 m. Their proximity indicates spatial consistency but does not establish that the observations correspond to the same sample location or identify the exact onset of flashing.

Discussion

Production Decline Shows Limited Fit to an Exponential Baseline

The low coefficient of determination does not independently demonstrate that scaling caused the production decline. Changes in wellhead conditions, operating strategies, reservoir pressure, feed-zone contributions, and measurement variability may also affect production. The R^2 value of 0.3825 indicates limited agreement with the selected log-linear baseline but does not exclude natural reservoir depletion. The physical interpretation therefore draws on the findings presented in the Thermal-Hydraulic Wellbore Simulation, Geochemical Saturation Modeling, Hydraulic Restriction Assessment, and XRD and Downhole Video Observations subsections.

Thermodynamically Sensitive Interval Near 1000 m Depth

The measured PTS and simulated WellSim temperature profiles approached one another near 1,000 m on the depth axis in Figure 2. The manuscript identifies the interval of 950–1,050 m as an approximate zone surrounding this convergence. However, the depth reference for the PTS data requires verification before the two profiles can be compared on a common measured-depth basis. The WellSim output indicates mist flow throughout the modeled interval, with a steam mass fraction of 0.980 at 1,700 m measured depth. Consequently, the comparison could neither identify the onset of flashing nor establish a specific calcite deposition zone.

Reported Carbonate Supersaturation Under the Modeled Conditions

Calcite is the carbonate mineral phase supported by the illustrated XRD evidence. The positive modeled SI is consistent with the potential for calcite precipitation. However, the incomplete definition of the geochemical solution and the mismatch between the modeled and reported pressure–temperature conditions prevent a definitive in situ thermodynamic interpretation. The PHREEQC output and mineralogical identification provide complementary forms of evidence; neither independently validates the undocumented input parameters of the other.

In this study, geochemical supersaturation contributes to a cautious diagnosis alongside the observed production behavior, the identified thermodynamically sensitive interval, and the hydraulic simulation scenarios. General mechanisms of mineral scaling have been reviewed by (Zhao et al., 2023). Nevertheless, the present simulation output does not establish a measured CO_2-degassing pathway or demonstrate that scaling was the dominant cause among the possible mechanisms contributing to production decline.

Hydraulic Response to the Combined Diameter and Roughness Scenario

The increased pressure gradients in the simulated scenario demonstrate how a narrower and rougher flow path can increase hydraulic resistance. Because the inner diameter and wall roughness were modified simultaneously, the results represent their combined effects. Without information on the restriction length, a discharge comparison under fixed operating conditions, or measured pressures before and after cleaning, the simulated pressure-gradient increase cannot be converted into an actual production loss or attributed exclusively to a reduction in flow area.

This distinction is consistent with the coupled treatment of compositional uncertainty and hydraulic efficiency discussed by (Shoeibi Omrani et al., 2025). The reported scenarios establish the hydraulic plausibility of flow restriction and indicate a potential priority for inspection. However, independently calibrated assessments of geometric and roughness effects remain necessary for designing appropriate interventions.

Published Deposit Evidence and Its Relevance to Well X

The observations from Patuha demonstrate that calcite deposition can occur in a vapor-dominated geothermal well. Their relevance to Well X is comparative because the available records do not establish a direct connection between the published specimen and video footage and the Well X case dataset. Consequently, the numerical proximity between the published video observation depth and the interval investigated in Well X provides insufficient evidence to establish a shared deposition zone or mechanism.

Integrated Interpretation of the Scaling Mechanism

The production regression exhibited a weak fit, the temperature profiles converged near an approximately defined thermodynamically sensitive interval, the supplied geochemical output indicated carbonate supersaturation, and the combined hydraulic simulation scenario produced increased pressure gradients. The XRD and DHV observations provided mineralogical and visual evidence of calcite deposition in the cited source. Collectively, these observations support a coherent diagnostic interpretation, subject to uncertainties in model reconstruction and the attribution of secondary evidence to Well X.

A plausible mechanism involves changes in residual-liquid chemistry that favor calcite precipitation, followed by mineral deposition that reduces the available flow area and increases hydraulic resistance. The reported PHREEQC output and hydraulic simulation scenarios illustrate different aspects of this proposed mechanism under their respective assumptions. However, the available records do not establish that this sequence occurred in Well X or quantify its contribution to production impairment. Reservoir evolution and changes in operating conditions remain plausible alternative explanations for the observed production trend.

The principal contribution of this study is a transparent, single-well synthesis of production, thermal, geochemical, hydraulic, and deposit-related evidence. The findings support targeted inspection near the identified thermodynamically sensitive interval and specify the additional records required to test the proposed interpretation. However, the study does not

supersede previous coupled modeling approaches or establish a unique cause of production decline.

CONCLUSION

The analysis of Well X supports calcite scaling as a plausible contributor to production impairment. The exponential baseline exhibited a limited fit (R^2=0.3825), while the temperature comparison indicated approximate profile convergence near 1,000 m measured depth. The modeled wellbore was already in mist flow at the deepest simulation boundary; therefore, the observed convergence could not establish the onset of flashing. The combined diameter-and-roughness scenario increased the total frictional and accelerational pressure gradient from 211.67 to 317.32 Pa/m, illustrating how a narrower and rougher flow path could increase hydraulic resistance and potentially impede production.

Confirmation requires Well X deposit records that establish a direct connection between mineral identification, sample recovery, and downhole imagery and the case dataset. Further investigations should verify the production measurements and PTS depth reference, reconstruct the PHREEQC inputs under matched pressure and temperature conditions, and evaluate the effects of diameter and wall roughness independently under fixed boundary conditions. Production and pressure measurements collected before and after any scale-removal operation under comparable operating conditions would also help quantify the contribution of scaling relative to reservoir-related and operational changes.

ACKNOWLEDGEMENT

The authors thank Politeknik Energi dan Mineral Akamigas (PEM Akamigas), Ministry of Energy and Mineral Resources (KESDM), Republic of Indonesia, for academic support.

AUTHOR CONTRIBUTION STATEMENT

Akhmad Sofyan contributed to the conceptualization and methodology of the study and to the interpretation of the findings on calcite scaling. Trisya Amanda Nur Rahma contributed to data curation, analysis of the production decline, and preparation of the original manuscript draft. Kristofol Waas contributed to the interpretation of the wellbore simulation and hydraulic scenarios and to the preparation of the figures and tables.

REFERENCES

Allan, G., Pogacnik, J., Siega, F., & Addison, S. (2019). Wellbore simulation to model calcite deposition on the Ngatamariki geothermal field, NZ. *Proceedings of the 44th Workshop on Geothermal Reservoir Engineering*. https://pangea.stanford.edu/ERE/db/GeoConf/papers/SGW/2019/Allan.pdf

Boch, R., Leis, A., Haslinger, E., Goldbrunner, J. E., Mittermayr, F., Fröschl, H., Hippler, D., & Dietzel, M. (2017). Scale-fragment formation impairing geothermal energy production: Interacting H_2S corrosion and $CaCO_3$ crystal growth. *Geothermal Energy*, *5*, 4. https://doi.org/10.1186/s40517-017-0062-3

Bu, X., Jiang, K., Wang, X., Liu, X., Tan, X., Kong, Y., & Wang, L. (2022). Analysis of calcium carbonate scaling and antiscaling field experiment. *Geothermics*, *104*, 102433. https://doi.org/10.1016/j.geothermics.2022.102433

Cao, B., Ma, Y., Liu, M., Li, S., Tian, H., & Feng, G. (2024). Predictions of locations of flash point and calcite scaling of geothermal fluids in wellbore by chemical and thermodynamic simulations. *Geothermics*, *121*, 103057. https://doi.org/10.1016/j.geothermics.2024.103057

Hassani, K., & Zheng, W. (2025). A review of recent advances in mineral scaling in geothermal energy systems: mechanisms, mitigation, and case studies. *Environmental Earth Sciences*, *84*(14), 418.

Hörbrand, T., Baumann, T., & Moog, H. C. (2018). Validation of hydrogeochemical databases for problems in deep geothermal energy. *Geothermal Energy*, *6*, 20. https://doi.org/10.1186/s40517-018-0106-3

Jamero, J., Zarrouk, S. J., & Mroczek, E. (2018). Mineral scaling in two-phase geothermal pipelines: Two case studies. *Geothermics*, *72*, 1–14.

https://doi.org/10.1016/j.geothermics.2017.10.015

Khasani, Deendarlianto, & Itoi, R. (2021). Numerical study of the effects of CO_2 gas in geothermal water on the fluid-flow characteristics in production wells. *Engineering Applications of Computational Fluid Mechanics*, *15*(1), 111–129. https://doi.org/10.1080/19942060.2020.1862709

Köhl, B., Elsner, M., & Baumann, T. (2020). Hydrochemical and operational parameters driving carbonate scale kinetics at geothermal facilities in the Bavarian Molasse Basin. *Geothermal Energy*, *8*, 26. https://doi.org/10.1186/s40517-020-00180-x

Lei, H., Xie, Y., Li, J., & Hou, X. (2023). Modeling of two-phase flow of high temperature geothermal production wells in the Yangbajing geothermal field, Tibet. *Frontiers in Earth Science*, *11*, 1019328. https://doi.org/10.3389/feart.2023.1019328

Lu, P., Zhang, G., Apps, J., & Zhu, C. (2022). Comparison of thermodynamic data files for PHREEQC. *Earth-Science Reviews*, *225*, 103888. https://doi.org/10.1016/j.earscirev.2021.103888

Quinao, J. J., Buscarlet, E., & Siega, F. (2017). Early identification and management of calcite deposition in the Ngatamariki geothermal field, New Zealand. *Proceedings of the 42nd Workshop on Geothermal Reservoir Engineering*. https://pangea.stanford.edu/ERE/db/IGAstandard/record_detail.php?id=27971

Shoeibi Omrani, P., Poort, J., Barros, E. G. D., de Zwart, H., Machado, C. G., Wasch, L., Twerda, A., Rijnaarts, H. H. M., & Shariat Torbaghan, S. (2025). A probabilistic model-based approach to assess and minimize scaling in geothermal plants. *Geothermal Energy*, *13*, 9. https://doi.org/10.1186/s40517-025-00336-7

Sofyan, A., Bujang, Y. D. G., & Suranta, B. Y. (2023). Heat loss effect analysis by using JIWAFlow wellbore simulation in geothermal field Well-Y. *AIP Conference Proceedings*, *2730*(1), 20116. https://doi.org/10.1063/5.0120544

Sofyan, A., Jaya, R., Susanto, H., Njeru, R. M., Bozsó, G., & Szanyi, J. (2025). Scale treatment planning using broaching method in a vapor-dominated geothermal Well X at Kamojang geothermal field. *Eng*, *6*(4), 67. https://doi.org/10.3390/eng6040067

Sujarmaitanto, H., Wardana, A. P., Iskandar, C., Sesesega, R. S., & Nurpratama, M. I. (2024). Insights on the water produced from a vapor-dominated system at Patuha geothermal field, Indonesia. *Proceedings of the 49th Workshop on Geothermal Reservoir Engineering*. https://pangea.stanford.edu/ERE/db/GeoConf/papers/SGW/2024/Sujarmaitanto.pdf

U.S. Geological Survey. (2025). PHREEQC version 3 [Computer software]. https://www.usgs.gov/software/phreeqc-version-3

Wahba, A., Khattab, H., Tantawy, M., & Gawish, A. (2022). Modern decline curve analysis of unconventional reservoirs: A comparative study using actual data. *Journal of Petroleum and Mining Engineering*, *24*(1). https://doi.org/10.21608/jpme.2022.128147.1123

Wanner, C., Eichinger, F., Jahrfeld, T., & Diamond, L. W. (2017). Causes of abundant calcite scaling in geothermal wells in the Bavarian Molasse Basin, Southern Germany. *Geothermics*, *70*, 324–338. https://doi.org/10.1016/j.geothermics.2017.05.001

Zhao, H., Huang, Y., Deng, S., Wang, L., Peng, H., Shen, X., Ling, D., Liu, L., & Liu, Y. (2023). Research progress on scaling mechanism and anti-scaling technology of geothermal well system. *Journal of Dispersion Science and Technology*, *44*(9), 1657–1670. https://doi.org/10.1080/01932691.2022.2033625